nature communications

Article

https://doi.org/10.1038/s41467-025-61845-4

An all-inorganic three-dimensional polyoxoniobate framework with ppb-level chemiresistive sensing for ammonia

Received: 15 January 2025

Accepted: 2 July 2025

Zheng-Wei Guo[1,3], Yan-Huang Yan[1,3], Yi Chen[1], Yi-Ying Li[1], Xin-Xiong Li[1], Cai Sun[1,2] & Shou-Tian Zheng[1,2]

Fabrication of gas sensors with high sensibility appears particularly important due to the urgent demand for toxic gases monitoring in public safety and atmosphere detection, especially for the detection requirement of ultra-low concentration gases. Here, we present a rare three-dimensional (3D) all-inorganic polyoxoniobate (PONb) framework based on $\{Cu_4@Nb_{29}\}$ secondary building units linked with both tetranuclear $\{Cu_4(OH)_5\}$ clusters and mononuclear $[Cu(H_2O)]^{2+}$ units. Remarkably, this 3D PONb framework exhibits an ultrasensitive response to NH_3 with a lowest limit of detection of 1.64 ppt up to now. Furthermore, the NH_3 induced single-crystal-to-single-crystal transformation as well as density functional theory analysis reveal that the strong coordination affinity of $[Cu(H_2O)]^{2+}$ linker for NH_3, along with more injection of charge into the framework, results in a ultrasensitivity chemiresistive responses to NH_3, at atomic-level insight.

The identification and detection of harmful gases are crucial for public safety, environmental protection, and medical diagnosis[1–3]. Ammonia (NH_3), widely used as a feedstock in the production of chemicals and fertilizers, is also a corrosive toxic gas that poses significant health risks with long-term exposure[4,5]. Thus, real-time monitoring of NH_3 concentration is essential for safeguarding both the environmental and health protection. Current detection methods, such as gas chromatography and mass spectrometry, can effectively detect trace gases. However, their large size and high cost limit their practical application[6]. This has led researchers to explore alternative techniques for sensitive identification and detection of NH_3.

Chemiresistive sensing technology has gained widespread attention as a promising alternative for gas detection due to its low cost, compact size, and robust real-time monitoring capabilities[7,8]. Numerous chemiresistive sensors responsive to NH_3 have been continuously developed, including those made from metal oxides[8,9], carbon-based materials[10,11], conductive polymers[12,13], and metal-organic frameworks (MOFs)[14]. However, current NH_3 sensors still face challenges such as low sensitivity, poor stability and high operating temperature, leading to poor recyclability and significant application limitations[15,16]. Therefore, developing new, robust sensing materials capable of detecting trace amounts of NH_3 is of great scientific significance.

All-inorganic 3D polyoxometalate (POM) frameworks are porous, purely inorganic molecular metal oxide networks built from POM secondary building units (SBUs) and metal linkers via covalent or coordination bonds. Noted that the metal linkers generally exclude alkali and alkaline earth metals, as they primarily interact with POMs through electrostatic forces. Such unique materials bridge the gap between zeolites and MOFs, exhibiting potential as chemiresistive gas-sensing materials. Moreover, they feature high stability, which is crucial in the presence of corrosive and coordinating gases like NH_3, which often cause structural degradation of MOFs by attacking their metal nodes[17,18]. Conversely, the high-charge POM SBUs within the all-inorganic 3D POM frameworks offer robust electrostatic interactions with metal linkers, thereby reinforcing the metal-oxo bonds. On the other hand, compared to zeolites, all-inorganic 3D POM frameworks possess greater flexibility in structural design, allowing them to be tailored for NH_3

---

[1]Fujian Provincial Key Laboratory of Advanced Inorganic Oxygenated Materials, College of Chemistry, Fuzhou University, Fuzhou, Fujian, China. [2]State Key Laboratory of Chemistry for NBC Hazards Protection, College of Chemistry, Fuzhou University, Fuzhou, Fujian, China. [3]These authors contributed equally: Zheng-Wei Guo, Yan-Huang Yan. e-mail: csun@fzu.edu.cn; stzheng@fzu.edu.cn

responsiveness by utilizing topological and reactivity principles similar to those in MOFs, through modifications to either the metal linkers or POM SBUs. Consequently, the all-inorganic 3D POM frameworks hold promise as high-performance chemiresistive NH_3 sensing materials, despite the fact that their performance in gas sensing has yet to be explored.

Notably, the acquisition of the all-inorganic 3D POM frameworks is not easy due to the scarcity of effective synthesis strategies. To date, only a small dozen of different structural types have been reported[19–25], significantly lagging behind the development of other porous materials such as zeolites and MOFs with hundreds and thousands of configurations, respectively. The known all-inorganic 3D POM frameworks are primarily based on polyoxotungstates, polyoxomolybdates and polyoxovanadates, with representative examples including frameworks constructed from POM SBUs like $\{Sn_9Si_2W_{18}\}$[20], $\{P_8W_{48}\}$[21], $\{P_5W_{30}\}$[22], $\{ZnMo_{12}\}$[23], and $\{V_{18}O_{42}(SO_4)\}$[24]. These materials exhibit highly intriguing redox properties, adjustable electronic characteristics, and catalytic performances. Recently, we reported the first $\{Ln_{12}Nb_{72}\}$-based all-inorganic 3D polyoxoniobate framework FZU-1 and demonstrated its superior performance in selective adsorption and elution of radioactive Sr^{2+} ions[25,26]. Therefore, advancing research on the synthesis of all-inorganic 3D POM frameworks, which are in urgent need of development, and exploring their potentially fascinating properties are of considerable scientific interest.

In this work, we present a novel all-inorganic 3D POM framework material, $H_{13}Na_8K_{18}\{[Cu(H_2O)]_2[Cu_4(OH)_5]\text{-}[Cu_4P_2Nb_{29}O_{93}]_2\}\cdot 48H_2O$ (**FZU-2**), which is constructed from new-type polyoxoniobate (PONb) SBUs of $\{Cu_4P_2Nb_{29}O_{93}\}$ (denoted as $Cu_4@Nb_{29}$) bridged by both tetranuclear $\{Cu_4(OH)_5\}$ copper-hydroxy clusters and mononuclear $[Cu(H_2O)]^{2+}$ copper complexes. Further, based on the framework, we demonstrate for the first time the potential application of all-inorganic 3D POM frameworks in gas sensing. Notably, **FZU-2** not only exhibits high framework stability but also an exceptionally sensitive response to NH_3, with a remarkable lowest limit of detection (LOD) of 1.64 ppt at room temperature, surpassing all previously reported chemiresistive NH_3 sensing materials. Additionally, the reversible NH_3-triggered single-crystal-to-single-crystal (SCSC) structural transformation of **FZU-2** offers atomic-level insights into its NH_3 response behaviors and mechanisms. Moreover, NH_3 can also trigger a reversible vaporchromic phenomenon, which offers a visual recognition for NH_3 sensing.

Results and discussion

Structure of FZU-2

FZU-2 crystallizes in tetragonal space group *I*4/m and its all-inorganic 3D framework features some attractive characteristics. To begin with, as is well-known, the known structural types of PONbs are limited owing to synthetic challenges caused by narrow and strongly basic working pH region and the slight solubility of niobate species. Fascinatingly, the $Cu_4@Nb_{29}$ SUB exhibits a rare new type of PONb. As shown in Fig. 1a, $Cu_4@Nb_{29}$ exhibits a C_s-symmetry core-shell-type nanocluster with ca. $1.7 \times 1.2 \times 1.2\ nm^3$ in dimensions, which consists of a unique 29-nuclearity hollow heart-shaped $\{P_2Nb_{29}O_{93}\}$ PONb shell (Fig. 1b) enclosing a 4-nuclearity tetrahedral $\{Cu_4O_{16}\}$ copper-oxygen cluster core (Fig. 1c).

The shell is comprised of two known Keggin-type trilacunary $\{A\text{-}\alpha\text{-}PNb_9O_{34}\}$ PONbs[27], and an unusual C_{2v}-symmetric basket-shaped $\{Nb_{11}O_{43}\}$ PONb unit (Fig. 1d). The $\{Nb_{11}O_{43}\}$ unit consists of three distinct types of Nb-polyhedra: six NbO_6 octahedra, four NbO_7 pentagonal bipyramids, and one NbO_5 pyramid. Every three NbO_6 octahedra are joined together through edge-sharing to form a $\{Nb_3O_{16}\}$ triangular triad. Each NbO_6 in the triad further connects to an NbO_7 pentagonal bipyramid also via edge-sharing, forming a tripod-like 6-nuclearity $\{Nb_6O_{28}\}$ unit. Two such tripodal units are arranged face-to-face and interconnected by sharing two NbO_7 pentagonal bipyramids, creating a basket-shaped $\{Nb_{10}O_{42}\}$ unit with a 6-ring cavity. This cavity is occupied by a 5-coordinate Nb^{5+} ion (NbO_5 pyramid), completing the basket-shaped $\{Nb_{11}O_{43}\}$ PONb unit (Supplementary Fig. 1). Finally, the two trilacunary $\{A\text{-}\alpha\text{-}PNb_9O_{34}\}$ PONbs are anchored to both sides of the basket-shaped $\{Nb_{11}O_{43}\}$ unit forming the overall 29-nuclearity hollow heart-shaped PONb shell with an internal spherical cavity of ca. 6.0 Å in diameter (Supplementary Fig. 2).

Pentagonal SBUs $\{M(M_5)\}$ (M = V, Mo, W, Nb) are of great interest in POM chemistry, as they are believed to be capable of forming large spherical or ring-shaped POMs analogous to fullerenes. Interestingly, the $\{P_2Nb_{29}O_{93}\}$ shell also can be described as a unique pentagonal $\{Nb(Nb_5)\}$-based tetrahedral cage of $\{Nb_{23}O_{79}\}$ capped by two $\{PNb_3O_{19}\}$ fragments (Supplementary Fig. 3). The $\{Nb_{23}O_{79}\}$ cage is made up of four $\{Nb(Nb_5)\}$ pentagonal SBUs, which exhibit two distinct types: two $\{Nb_6O_{27}\}$ and two $\{Nb_6O_{26}\}$ (Supplementary Fig. 4). The $\{Nb_6O_{27}\}$ displays a nearly planar structure, formed by five NbO_6 octahedra encircling a NbO_7 pentagonal bipyramid, whereas the $\{Nb_6O_{26}\}$ shows a curved structure, composed of four NbO_6 octahedra and one NbO_5 square pyramid surrounding a NbO_7 pentagonal

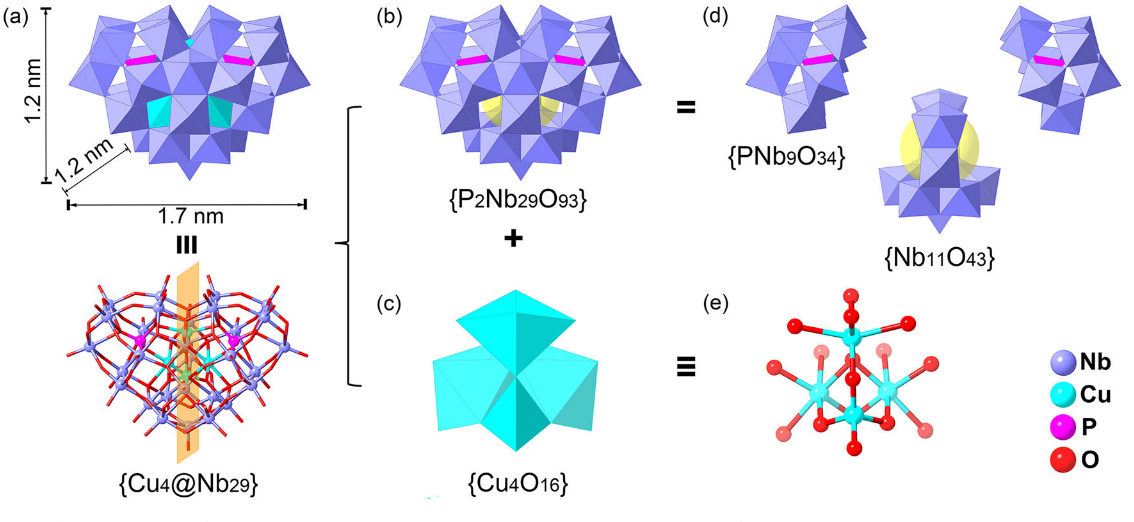

Fig. 1 | Secondary Building Units (SBUs). a Polyhedron representation of $Cu_4@Nb_{29}$ and the view of $Cu_4@Nb_{29}$ with a symmetry plane. **b** View of the structure of heart-shaped $\{P_2Nb_{29}O_{93}\}$ PONb shell. **c** Polyhedron representation of $\{Cu_4O_{16}\}$ core. **d** Polyhedron representations of tri-lacunary Keggin-type $\{A\text{-}\alpha\text{-}PNb_9O_{34}\}$ unit and basket-shaped $\{Nb_{11}O_{43}\}$ unit. **e** Ball and stick representation of $\{Cu_4O_{16}\}$ core.

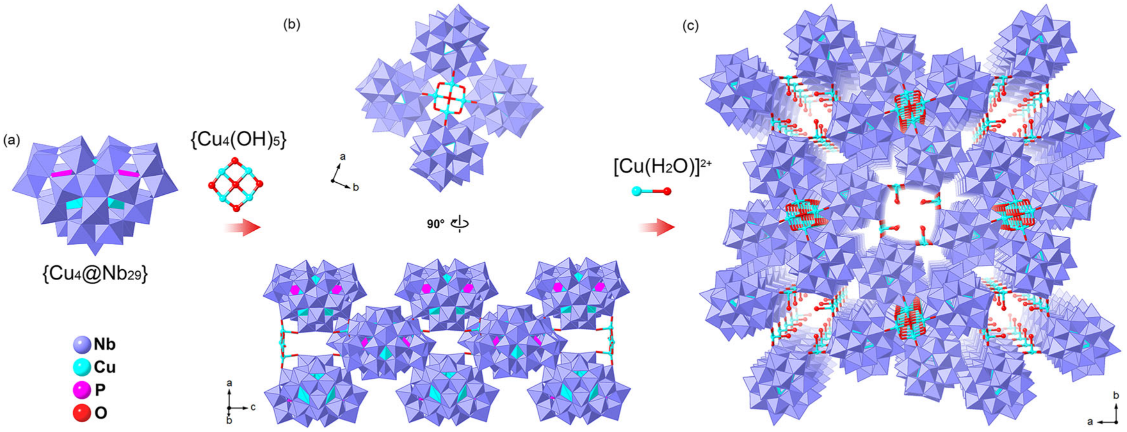

Fig. 2 | Structure of FZU-2. a View of the $Cu_4@Nb_{29}$ SBU. **b** View of the 4_2-symmetry 1D chain. **c** View of the extending 3D structure along *c* axis.

bipyramid (Supplementary Fig. 5). The two planar $\{Nb_6O_{27}\}$ SBUs form a C_{2v}-symmetry V-shaped dimer through two pairs of edge-sharing NbO_6 octahedra, while two $\{Nb_6O_{26}\}$ SBUs form another kind of C_{2v}-symmetry V-shaped dimer via both two pairs of edge-sharing NbO_6 octahedra and a shared NbO_5 square pyramid. These two types of V-shaped dimers connect with each other in a face-to-face and mutually perpendicular manner through edge-sharing and vertex-sharing, fusing into a tetrahedron-like cage (Supplementary Fig. 4).

It is noteworthy that the PONb $[H_{10}Nb_{31}O_{93}(CO_3)]^{23-}$ (Nb_{31}), first reported by Cronin et al.[28], also incorporates four $\{Nb(Nb_5)\}$ pentagonal SBUs. In Nb_{31}, these four pentagonal SBUs are interconnected to form an *E*-symmetric non-closed structure (Supplementary Fig. 6), whose topological configuration is markedly distinct from our closed C_{2v}-symmetric tetrahedral $\{Nb_{23}O_{79}\}$ cage. To our knowledge, the $\{Nb_{23}O_{79}\}$ motif presents the smallest cage known to date that is entirely constructed from pentagonal SBUs of $\{M(M_5)\}$.

The $\{Cu_4O_{16}\}$ core can be viewed as a tetrahedral copper-oxygen cluster composed of three CuO_6 octahedra and one CuO_4 tetrahedron (Fig. 1e). The three octahedral Cu^{2+} ions are hold together by a μ_3-O atom to form a nearly coplanar triangle. The remaining tetrahedral Cu^{2+} ion caps to the triangular plane through three μ_2-O atoms, forming the tetrahedral $\{Cu_4O_{16}\}$ core (Supplementary Fig. 7). It is noted that the $\{Cu_4O_{16}\}$ core is disordered into two sets of tetrahedral structures, as illustrated specifically in Supplementary Fig. 8. The Cu-O bond lengths of all CuO_6 octahedra and the CuO_4 tetrahedron are in the ranges of 1.888(1)–2.473(1) Å and 1.614(1)–1.866(1) Å, respectively (Supplementary Table 1). Some Cu-O bond distances of CuO_6 octahedra are significantly elongated or shortened due to the Jahn-Teller effect of Cu^{2+}. The $\{Cu_4O_{16}\}$ core is encapsulated in the central cavity of the $\{P_2Nb_{29}O_{93}\}$ shell, leading to a core-shell PONb of $Cu_4@Nb_{29}$.

Apart from being based on novel $Cu_4@Nb_{29}$ SBUs, **FZU-2** is also an interesting 3D all-inorganic POM framework featuring mixed inorganic linkers. As shown in Fig. 2, there are two types of copper linkers in the framework: one is tetranuclear $\{Cu_4(OH)_5\}$ copper-hydroxy cluster, and the other is $[Cu(H_2O)]^{2+}$ complex. Unlike the C_s-symmetrical arrangement of the four Cu^{2+} ions in the $\{Cu_4O_{16}\}$ core, the four Cu^{2+} ions in the $\{Cu_4(OH)_5\}$ linker adopt a C_{4d}-symmetrical arrangement, interconnected by one μ_4-OH and four μ_2-OH ligands to form an uncommon planar square configuration (Supplementary Fig. 9). All the OH groups and H_2O ligand are confirmed by bond valence sum calculations (Supplementary Table 2)[29].

In the framework, the $\{Cu_4(OH)_5\}$ linkers connect $Cu_4@Nb_{29}$ SBUs along the *c*-axis, forming a 4_2-symmetry 1D chain of $-(Cu_4@Nb_{29})_2-Cu_4(OH)_5-(Cu_4@Nb_{29})_2-Cu_4(OH)_5-$ (Supplementary Figs. 10, 11). In this chain, every four adjacent $Cu_4@Nb_{29}$ SBUs are arranged in a tetrahedral fashion and unified by a $\{Cu_4(OH)_5\}$ linker positioned at the tetrameric center (Supplementary Fig. 12). Inside this tetrameric fragment, each Cu^{2+} ion, while coordinating with one μ_4-OH and two μ_2-OH groups, also bonds to two terminal oxo atoms from a $Cu_4@Nb_{29}$, forming a 5-coordinate square pyramid with Cu-O bond lengths ranging from 1.897(1)-2.503(3) Å.

Complementing the bridging direction of the $\{Cu_4(OH)_5\}$ linkers along the *c*-axis, the $[Cu(H_2O)]^{2+}$ complexes crosslink the 1D chains of $-(Cu_4@Nb_{29})_2-Cu_4(OH)_5-(Cu_4@Nb_{29})_2-Cu_4(OH)_5-$ along the *a*- and *b*-axis directions, resulting in the formation of the overall all-inorganic 3D POM framework with 1D square channels along the *c*-axis direction (Fig. 2 and Supplementary Fig. 13). Each square pore channel, possessing a pore size of $1.2 \times 1.2\ nm^2$, is defined by four 1D chains in a C_4-symmetry arrangement, where the adjacent chains are bridged by one $[Cu(H_2O)]^{2+}$ complex with Cu-O bond lengths of 1.918(1) Å and 2.422(1) Å (Supplementary Fig. 14). Notably, in the absence of the $\{Cu_4(OH)_5\}$ linkers, the $[Cu(H_2O)]^{2+}$ complexes would solely be able to link $Cu_4@Nb_{29}$ SBUs into discrete planar tetramers with C_{4h}-symmetry (Supplementary Fig. 15), which are stacked in parallel along the *c*-axis with a spacing of 4.5 Å between adjacent tetramers. Analogous to the square pyramid configuration displayed by the Cu^{2+} ions in the $\{Cu_4(OH)_5\}$ linker, the Cu^{2+} ion of $[Cu(H_2O)]^{2+}$ linker form a 5-coordinate square pyramid by coordinating with one water ligand and four terminal oxo atoms from two $Cu_4@Nb_{29}$ SBUs. Interestingly, the water ligands directed towards the pore channels, along with the nanoscale pore sizes and robust purely inorganic 3D framework, endow **FZU-2** with the potential for gas sensing.

Characterization and NH_3 detection

The purity of as-synthesized **FZU-2** were confirmed by powder X-ray diffraction (PXRD, Supplementary Fig. 16), IR (Supplementary Fig. 17), and elemental analyses (see the Experimental Section in the Supporting Information). Variable-temperature PXRD tests show that **FZU-2** exhibits high thermal stability, maintaining its structural integrity up to 200 °C (Supplementary Fig. 18). Furthermore, the samples remain structurally stable after soaking in aqueous solutions with a broad pH range of 4–13 or common organic solvents for 1 day, demonstrating high chemical stability (Fig. 3a). Notably, compared to the all-inorganic 3D frameworks constructed from acid-stable POMs of V, Mo, and W, the all-inorganic 3D frameworks based on base-stable PONbs have superior stability under strongly basic conditions. This is particularly advantageous for gas-sensing research and applications in basic atmospheres.

Due to the unique and fascinating structural features, as well as the high stability of **FZU-2**, we have spearheaded the exploration of the potential gas-sensing properties of 3D all-inorganic POM frameworks, specifically targeting NH_3, a basic gas, as the subject of our research.

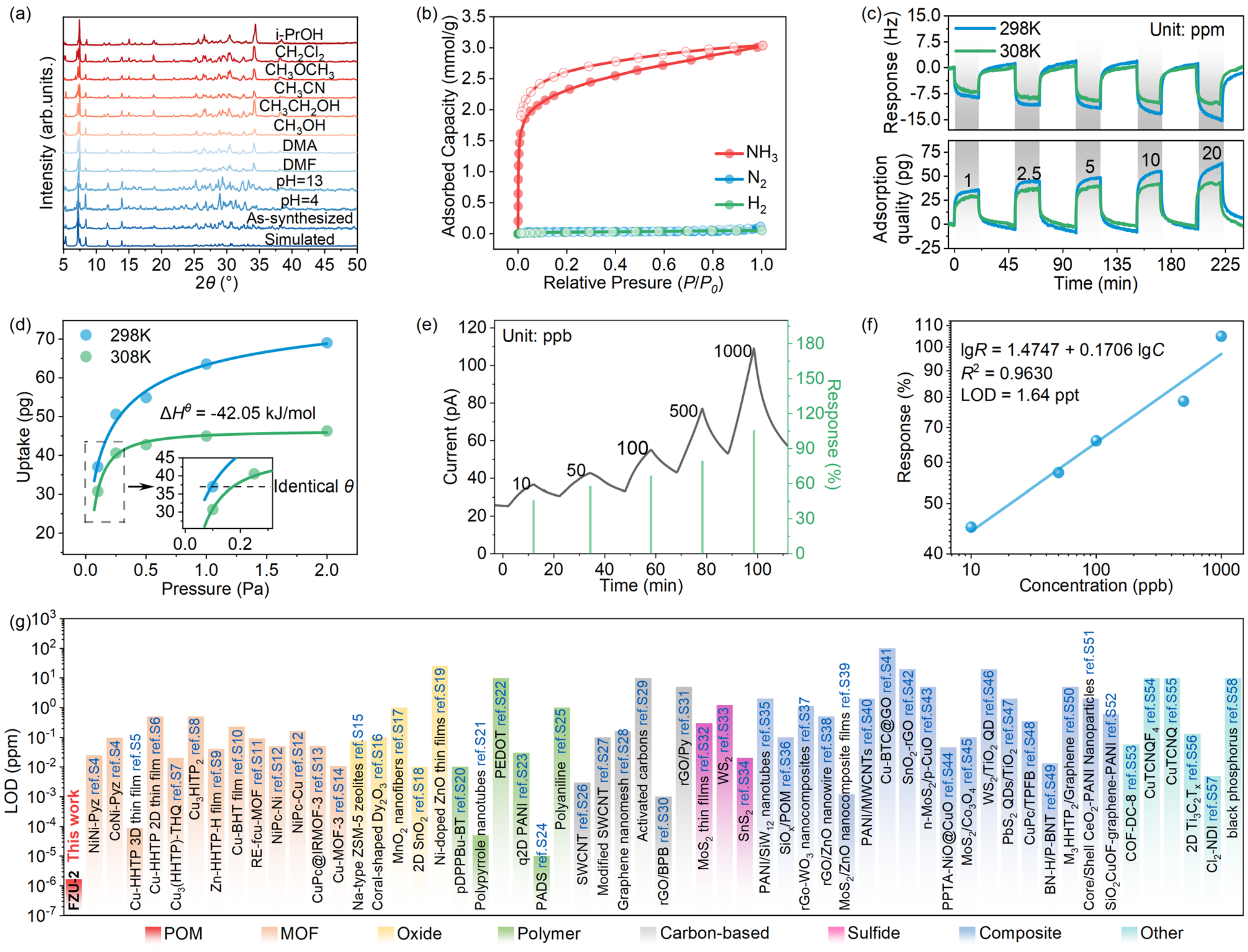

Fig. 3 | NH_3 detection. a PXRD patterns after soaking in different solvents for 1 day. **b** Adsorption and desorption isotherms for NH_3 at 298 K with N_2 and H_2 for comparison. **c** Microravimetric NH_3 sensing responses and adsorption quality at 298 K and 308 K. The quantitative relationship is that of 1 pg mass being equivalent to the frequency change of 0.24 Hz. **d** The isotherms of the **FZU-2**-loaded resonant-cantilever to NH_3 of various trace-level concentrations. **e** Concentration-dependent response-recovery curves. **f** Response-concentration log-log plots. **g** Comparison of LOD of various NH_3 responsive materials at RT.

The NH_3 sorption experiment for activated samples of **FZU-2** are conducted at 298 K. It could be seen from the adsorption curve (Fig. 3b) that **FZU-2** exhibits type I isotherm[30], with steep uptakes at low relative pressure, follows by a gradual decrease in adsorption rate with the total NH_3 uptake of 3.02 mmol · g^{-1} at 1 bar. This result indicates that **FZU-2** has porous characteristics and sensitivity to low concentrations of NH_3. The PXRD pattern after NH_3 adsorption-desorption experiment further confirm the structural stability of **FZU-2** (Supplementary Fig. 19). Notably, **FZU-2** hardly adsorbs N_2 and H_2 under the same conditions, and such good adsorption selectivity perfectly meets the NH_3 detection requirements in the Haber-Bosch processes[17].

A microgravimetric experiment is conducted to further evaluate the sensing capability of **FZU-2** for detecting trace NH_3 from a thermodynamic insight. A resonant microcantilever sensor is employed for real-time quantitative detection of the periodic adsorption-desorption process when exposed to trace NH_3, with dry air as the carrier gas. The NH_3 molecules trapped by **FZU-2** cause an increase in mass, which can be detected by a drop in frequency. As shown in Fig. 3c, the dropping signal of frequency gradually enlarges with the rise in NH_3 concentration. At 298 K, the response signals are 8.89–16.57 Hz for the NH_3 concentration in the range of 1–20 ppm, indicating that **FZU-2** is sensitive to NH_3 at the ppm level. A similar gravimetric experiment is performed at a higher temperature of 308 K, where the sensing signal is lower than that at 298 K for the same NH_3 vapor concentration, indicating that increasing the temperature is not conducive to the adsorption of NH_3 (Supplementary Tables 3, 4). According to two fitting isotherms (Fig. 3d) and Clausius-Clapeyron equation, the standard enthalpy (ΔH^θ) of adsorption can be calculated as −42.05 kJ · mol^{-1}. This indicates a combined contribution of chemisorption and physisorption, which is suitable for a chemiresistor according to reported literatures[31]. The well-fitting linear plot of p/Γ versus p, with an R^2 of 0.996 according to Langmuir equation, is used to calculate the adsorption-desorption equilibrium constant K, determined to be as 6.20 Pa^{-1} (Supplementary Fig. 20). Notably, the negative standard Gibbs free energy (ΔG^θ) value of −33.05 kJ · mol^{-1} for **FZU-2** implies a spontaneous NH_3 adsorption process (Supplementary Table 5). Moreover, the calculated negative entropy (ΔS^θ) of −30.18 J · K^{-1} indicates a decreased degree of freedom after NH_3 adsorption, and the NH_3 molecules are restricted from their original free movement in space to the surface. These thermodynamic parameters further demonstrate the potential of **FZU-2** for RT NH_3 sensing.

A chemiresistive sensor based on **FZU-2** powder is fabricated using the drop-coating method onto interdigital electrodes (Supplementary Fig. 21). Trace NH_3 sensing measurements are performed in a homemade dynamic sensing setup at 298 K with dry air as the carrier gas (Supplementary Fig. 22). As shown in Fig. 3e, the current significantly increases upon exposure to NH_3, which is the typical behavior of a n-type semiconductor[32]. The current curve presents a typical real-time response-recovery curve over a broad concentration range of

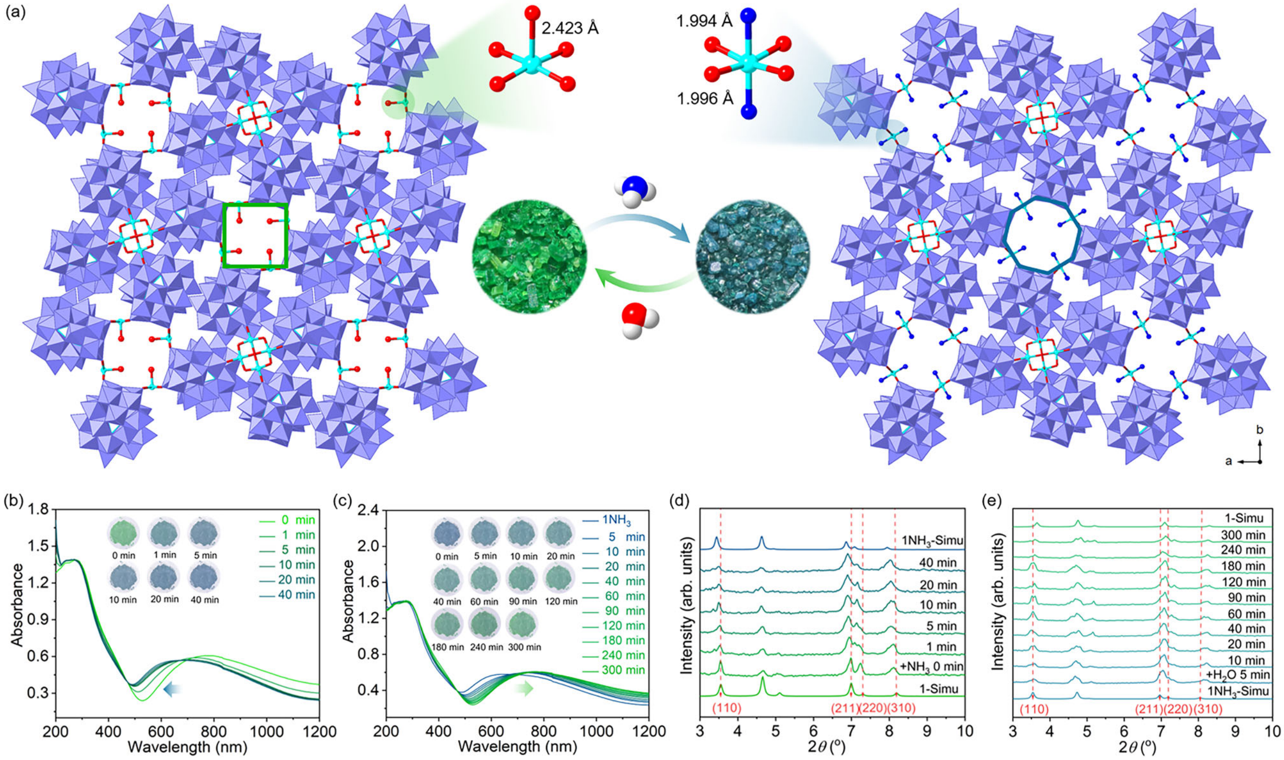

Fig. 4 | Single-crystal to single-crystal (SCSC) structural transformation. a The NH_3/H_2O-induced vaporchromism accompany by crystal phase transformation. **b**, **c** Time-dependent adsorption spectra of NH_3 adsorption and desorption processes. **d**, **e** Time-dependent PXRD patterns during NH_3 adsorption and desorption processes. Atom color: oxygen (red), copper (cyan), nitrogen (blue), hydrogen (gray).

0.01–1 ppm. The response, defined as I-I_0/I_0, increases with rising NH_3 concentration, where I_0 and I are the average current levels of dry air and different concentrations of NH_3, respectively. The result indicates that **FZU-2** is suitable for real-time monitoring of NH_3. The response at 1 ppm NH_3 is estimated up to be 105%, exceeding most NH_3 sensing materials (Supplementary Table 6). Moreover, the response-concentration log-log plots of **FZU-2** toward NH_3 shows good linearity in the range of 0.01–1 ppm, with an R^2 of 0.9630 (Fig. 3f). The theoretical limit of detection (LOD) is calculated to be ~1.64 ppt from the fitted linear equation by setting the response to be 10%, indicating high sensitivity of **FZU-2** toward NH_3. Notably, **FZU-2** represents the lowest LOD among all reported RT chemiresistive NH_3 sensing materials (Fig. 3g and Supplementary Table 6). Furthermore, **FZU-2** demonstrates excellent selectivity toward nine common interfering gases, including CH_4, C_2H_6, C_2H_4, C_2H_2, CH_3COCH_3, H_2S, CO_2, SO_2, and NO_2 (Supplementary Fig. 23). The response to 1 ppm NH_3 with low coefficient of variation of 5.2 % over five consecutive cycles (Supplementary Fig. 24) show good repeatability of **FZU-2**. Relative humidity-dependent current response tests indicate that low to moderate humidity levels (≤60%) minimally affect the NH_3 sensing performance of **FZU-2**, suggesting its suitability for applications in such scenarios (Supplementary Fig. 25)[33–35].

Single-crystal transformation and DFT calculation

To reveal the reason of ultrasensitive response toward NH_3, we investigate NH_3 induced structural transformation behavior of **FZU-2**. As shown in Fig. 4a, the as-synthesized green crystalline sample of **FZU-2** turned blue after exposure to saturated NH_3 vapor. Time-dependent absorption spectra indicate that the characteristic d-d transition peak of Cu^{2+}, centered at 800 nm, shifts blue with increasing exposure time, indicating a change in the coordination environment of Cu^{2+}. After exposure for 40 min, the center of peak shifts blue to 600 nm, and further extension of the exposure time results in negligible change in the absorption spectrum, indicating that the vaporchromism tends to be saturated (Fig. 4b). The colored state can remain stable for a long time under an inert atmosphere (Supplementary Fig. 26), but when exposed to a 55% humid atmosphere, it reversibly gradually returns to its initial state (Fig. 4c and Supplementary Fig. 26). The NH_3-induced SCSC transformation of **FZU-2** with high-quality single crystal X-ray diffraction (SXRD) data further provides an atomic-level insight into NH_3 response behavior. The colored crystalline sample, $H_{13}Na_8K_{18}\{[Cu(NH_3)_2]_2[Cu_4(OH)_5][Cu_4P_2Nb_{29}O_{93}]_2\}\cdot 30H_2O\cdot 6NH_3$ (**FZU-2NH$_3$**), maintains a similar all-inorganic 3D framework to **FZU-2** (Fig. 4a, Supplementary Fig. 27 and Supplementary Table 7). The presence and content of NH_3 in the **FZU-2NH$_3$** are verified through IR, XPS, and element analysis (Supplementary Table 8 and Supplementary Figs. 17, 28, 29). As shown in Fig. 4a, the H_2O ligand of each $(Cu(H_2O)O_4)$ is replaced by two NH_3 molecules, resulting in the transformation of the copper coordination geometry from the original 5-coordinate square pyramid $\{Cu(H_2O)O_4\}$ to a 6-coordinate octahedron $\{Cu(NH_3)_2O_4\}$. In contrast, the copper coordination environment of $\{Cu_4(OH)_5\}$ linkers remains unchanged. Due to NH_3 being a stronger field ligand compared to H_2O, the blue shift in the d-d transition absorption band of Cu^{2+} after NH_3 stimulation can be well explained. The change in the coordination environment of the $\{Cu(H_2O)O_4\}$ linker leads to a slight disturbance in the connections between adjacent SBUs. This disturbance causes the pore window transform from a nearly square shape to an octagonal shape. The change further results in a cell length variation of up to 3.1% in the *a*- and *b*-axis, which is significantly greater than the 0.5% variation in the *c*-axis direction.

Time-dependent PXRD data clearly display the dynamic change process. As shown in Fig. 4d, with increased exposure time to NH_3 atmosphere, the diffraction peaks of crystal face groups with non-zero *h* and *k* indices, such as (110), (211), (220), and (310), shift to the left. The interplanar spacing of (110), (211), (220), and (310) increases from

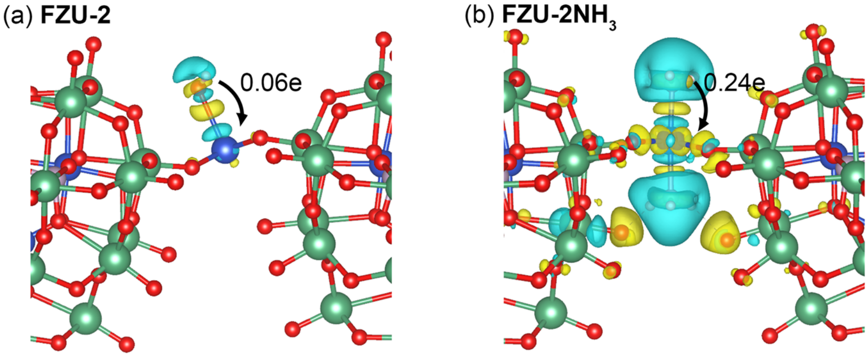

Fig. 5 | DFT calculation. a Charge density difference and Bader charge analysis for **FZU-2**. **b** Charge density difference and Bader charge analysis for **FZU-2NH$_3$**. Isosurfaces with yellow and blue isosurface levels being set at ±0.002 e/bohr^3, respectively. Atom color: niobium (green), oxygen (red), copper (blue).

23.54 Å, 12.27 Å, 11.77 Å and 10.52 Å, to 24.26 Å, 12.50 Å, 12.13 Å, and 10.85 Å, respectively (Supplementary Fig. 30). Similarly, SXRD (Supplementary Table 7) and PXRD data (Fig. 4e) further demonstrate that in a 55 % humid atmosphere, H_2O molecules will re-attack $[Cu(NH_3)_2]^{2+}$ linkers of **FZU-2NH$_3$**, restoring to original crystal (denoted as **FZU-2Recovered**). Density functional theory (DFT) calculations further elucidate the electronic structural changes during the adsorption response process. As shown in Fig. 5, the charge density difference analysis reveals that NH_3 adsorption induces a more pronounced charge transfer compared to H_2O adsorption, indicating stronger intermolecular interaction energies between NH_3 and the adsorption sites, aligning with the observed ultrasensitivity of **FZU-2** to NH_3. Additionally, Bader charge analysis demonstrates that these adsorbed gas molecules can transfer electrons to the PONb framework, consistent with the n-type semiconductor behavior of **FZU-2**. Specifically, an H_2O molecule transfers only 0.06e of charge to the framework, whereas an NH_3 molecule transfers as much as 0.24e, explaining the significant current increase observed during the NH_3 response process. Therefore, the ultrasensitivity of **FZU-2** to NH_3 in chemiresistive sensing is primarily due to the strong coordination affinity of $[Cu(H_2O)]^{2+}$ linker for NH_3, which leads to the dissociation of H_2O molecules and rapid uptake of the NH_3 to form Cu-N bonds, followed by expansion in the framework along both the *a* and *b* directions. This alteration of structure, along with the injection of charge from the gas molecules into the **FZU-2** framework, results in a corresponding change of conductivity.

In summary, we have prepared a rare all-inorganic 3D PONb framework of **FZU-2**, which possesses many fascinating features, including heart-shaped nanoscale PONb SBUs, mixed inorganic linkers, nanoporous channels, and high stability. Based on these characteristics, we selected corrosive and toxic NH_3 gas as the research target and explored, for the first time, the potential application of all-inorganic 3D POM frameworks in chemiresistive gas-sensing materials. Delightfully, **FZU-2** exhibits ultra-sensitivity to NH_3 at RT, with the lowest LOD among all reported RT chemiresistive NH_3 sensing materials. Furthermore, the high crystallinity and structural stability enabled us to understand the SCSC structural transformation details of **FZU-2** during NH_3 sensing through SXRD, thereby intuitively revealing its mechanism of sensitive response to trace NH_3 at the atomic level. This work not only enriches the family of rare all-inorganic 3D POM frameworks but also pioneers the potential application of such materials in the field of chemiresistive gas sensing, providing important insights and guidance for designing and developing novel and high-performance RT chemiresistive sensors.

Methods

Materials

Chemicals were used as purchased without further purification. Water was deionized and distilled before use.

Measurements

Powder XRD patterns were obtained using a RIGAKU-Miniflex II diffractometer with Cu K_α radiation ($\lambda = 1.54056$ Å). IR spectra were recorded on PerkinElmer Spectrum One FT-IR infrared spectrophotometer with pressed KBr pellets in the range of 4000–400 cm^{-1}. UV-vis spectra were measured using a SHIMADZU UV-2600. UV-vis spectrophotometer equipped with an integrating sphere attachment and $BaSO_4$ as reference. Inductively coupled plasma atomic emission spectrometry (ICP-AES) was performed on an Ultima2 spectrometer. X-ray photoelectron spectroscopy (XPS) was carried out using a XPS system (Thermo-Fisher, ESCLAB 250, USA).

Single-crystal structure analysis. Crystals were collected on a Bruker APEX II CCD area diffractometer equipped with a fine focus, 2.0 kW sealed tube X-ray source (Mo K_α radiation, $\lambda = 0.71073$ Å) operating at 175(2) K. The empirical absorption correction was based on equivalent reflections. The structures were solved by direct methods followed by successive difference Fourier methods. Computations were performed using SHELXTL and final full-matrix refinements were against F^2. The contribution of disordered solvent molecules to the overall intensity data of structure was treated using the SQUEEZE method in PLATON.

Synthesis of $K_{18}Na_8H_{13}\{[Cu(H_2O)]_2[Cu_4(OH)_5][Cu_4P_2Nb_{29}\text{-}\ O_{93}]_2\}\cdot 48H_2O$ (FZU-2). $K_7HNb_6O_{19}\cdot 13H_2O$ (0.295 g, 0.215 mmol) was dissolved in 8 mL distilled water followed by $Na_2HPO_4\cdot 7H_2O$ (0.118 g, 0.44 mmol) and $Cu(CH_3COO)_2\cdot H_2O$ (0.055 g, 0.275 mmol). The mixture vigorous stirred for about 1 h, then transferred to a 25 ml Teflon-lined stainless steel autoclave and heated at 200 °C for 96 h. After cooling to room temperature, green rod-shaped crystals suitable for X-ray crystallography were obtained. Yield: about 15 mg (35.9%, based on $K_7HNb_6O_{19}\cdot 13H_2O$). ICP analyses (based on dried sample) calcd (found %) for $H_{18}Na_8K_{18}Cu_{14}P_4Nb_{58}O_{191}$: Na, 1.77 (1.45); K, 6.79 (7.05); P, 1.20 (1.28); Cu, 8.58 (7.95); Nb, 52.00 (52.56). IR (KBr pellet): 3287(s), 1623(m), 1053(m), 1013(m), 865(s), 676(s), 586(s), 471(s).

Synthesis of $K_{18}Na_8H_{13}\{[Cu(NH_3)_2]_2[Cu_4(OH)_5][Cu_4P_2Nb_{29}O_{93}]_2\}\cdot 30H_2O\cdot 6NH_3$ (FZU-2NH$_3$). **FZU-2NH$_3$** is synthesized by exposing crystal samples of **FZU-2** to ammonia atmosphere for 0.5-1 h. The content of ammonia is determined by crystallographic data and elemental analysis. IR (KBr pellet): 3268(s), 1627(m), 1422(m), 1253(m), 1052(m), 1001(m), 865(s), 683(s), 585(s), 473(s).

Synthesis of $K_{18}Na_8H_{13}\{[Cu(H_2O)]_2[Cu_4(OH)_5][Cu_4P_2Nb_{29}\text{-}\ O_{93}]_2\}\cdot 44H_2O$ (FZU-2Recovered). Fresh blue-colored single crystals of **FZU-2NH$_3$** were placed in a small vessel then put in air (humidity: 55%) for over 4 h. The blue crystals of **FZU-2NH$_3$** gradually converted back into green crystals of **FZU-2** without disrupting the crystallographic order and still suitable for single-crystal X-ray diffraction analysis. ICP analyses (based on dried sample) calcd (found %): Na, 1.77 (1.48); K, 6.79 (7.23); P, 1.20 (1.25); Cu, 8.58 (7.96); Nb, 52.00 (52.60).

Synthesis discussion. In our study, we identified three key synthesis parameters that significantly influence the successful synthesis of **FZU-2**.

Firstly, Na_2HPO_4 is essential for the formation of **FZU-2**. It not only acts as a pH modulator, regulating the microenvironment of the reaction, but also serves as a source of heteroanions $\left(PO_4^{3-}\right)$, which function as templates to induce the formation of lacunary PONb-based building units.

Secondly, reaction temperature plays a crucial role in determining both the yield and crystallinity of the final product. Parallel experiments reveal that **FZU-2** cannot be obtained at temperatures below 160 °C, whereas crystalline products begin to form only when the temperature exceeds this threshold. As the temperature increases, both yield and crystallinity improve. We speculate that a higher reaction temperature facilitates the dissolution of raw materials, promotes precursor decomposition, and enhances the recombination of lacunary PONb-based building units, thereby driving the crystallization process.

Additionally, Cu^{2+} also play a crucial role in the construction of **FZU-2**. We explored the possibility of substituting Cu^{2+} with other transition metals, including Cr^{3+}, Mn^{2+}, Fe^{3+}, Co^{2+}, Ni^{2+}, and Zn^{2+}, under the same reaction conditions. However, only precipitates were observed in these cases. This is likely due to the limited solubility of these metal ions, which undergo hydrolysis under strongly alkaline conditions. In contrast, Cu^{2+} can form stable soluble complexes with hydroxide ions in such environments, thereby increasing its solubility and enabling its participation in the self-assembly process. Moreover, Cu^{2+} exhibits remarkable flexibility in coordination, forming various geometries, including the planar $[Cu_4(OH)_5]^{3+}$ linkers composed of four five-coordinated Cu^{2+} ions. The versatility in coordinating configurations is precisely why attempts to replace the Cu^{2+} ion with others have been unsuccessful to yield the same structure.

NH_3 sensing detection. The DC chemiresistive sensors were developed by drop coating the isopropanol suspension of **FZU-2** sample onto the silver interdigital electrodes. A mixture of **FZU-2** (50 mg) and isopropanol (100 μL) was stirred and ground for 10 min at RT to obtain a well-dispersed suspension, then the sensor was conveniently fabricated by drop coating the suspension (20 μL) onto the interdigital electrodes, then dried at RT. The sensing performances were conducted by a homemade setup (Supplementary Fig. 22), and the concentration of NH_3 in the analyte flow was controlled by a dynamic volumetric method and calibrated by a commercial instrument. Mass flow controllers (MFC, CS-200C, Beijing Sevenstar Qualiflow Electronic Equipment Manufacturing Co., Ltd., China) were utilized to control the flow rate (υ) of gas, MFC1 for bubbling gas (dry air for bubbling into the water), MFC2 for mixed gas (dry air for mixing with analyte gas), and MFC3 for dry air (blank measurement), MFC4 for analyte gas (analyte gas is mixed with dry air). The targeted NH_3 concentration (x) and humidity (RH) were produced by mixing the bubbling gas and mixed gas in a proper ratio and calculated by the following equation:

$$x = \frac{\upsilon_{MFC4}}{\upsilon_{\mathrm{MFC2}} + \upsilon_{MFC4}} \tag{1}$$

$$RH = \frac{\upsilon_{MFC1}}{\upsilon_{MFC2} + \upsilon_{MFC1}} \times 100\% \tag{2}$$

The sensor devices were placed in an opaque, sealed quartz chamber at room temperature, with dry air used as the carrier gas for the target gas. To eliminate interference from other gases, the sensor device was first purged with a constant flow of dry air at 200 sccm (mL/min) until the current stabilized. Once the target gas concentration was balanced in the gas mixer for 7 min, it was then introduced into the chamber. Various concentrations of the target gas were tested using a custom-built sensing setup. The gas-sensing experiments were conducted by monitoring changes in the DC current of the device under different target gas concentrations. The current was recorded using a Keithley 2636B System Sourcemeter, with a bias voltage of 1 V. The sensor response (R) and coefficient of variation (CV) were defined according to the following method:

$$R = \left(\frac{I_g}{I_0} - 1\right) \times 100\% \tag{3}$$

$$\mathrm{CV} = \frac{R_{SD}}{R_{average}} \times 100\% \tag{4}$$

where I_O is the initial current value of the sensor at dry air, and I_g is the steady state current of the sensor when exposed to different concentrations of target gas. Here, R_{SD} represents the relative standard deviation of the response, reflecting the degree of data dispersion; R_{average} indicates the average response value under the same concentration cycle, reflecting the central tendency of the data.

Microravimetric NH_3 sensing test. Microravimetric measurements were carried out using MEMS cantilever (LoC-TGA 3000) chips connected to the computer and a Molecular Adsorption Analyzer acquired from High-End MEMS Technology Co., Ltd. The powder of **FZU-2** was firstly dispersed in ethanol, then loaded onto the tip of a microcantilever chip using a cantilever microscope. After drying thoroughly at 70 °C, the adsorption of NH_3 was measured by detecting the vibration frequency of the cantilever beam in the range of 1–20 ppm.

Gas adsorption measurements. Gas adsorption isotherms were measured using a micromeritics 3flex adsorption analyzer or BSD adsorption instruments of Beishide Instrument Company. The samples were degassed at 100 °C for 6 h under high dynamic vacuum before measurement. For the measurement of NH_3, N_2 and H_2 adsorption, 60 mg, 200 mg and 200 mg samples were used, respectively. N_2 and H_2 isotherms were collected at 77 K, NH_3 isotherm was collected at 298 K.

Computational approaches

First-principles DFT simulations were performed using the VASP package. The electron exchange-correlation energies were treated by the generalized gradient approximation in the Perdew Burke Ernzerhof scheme[36]. In addition, the projection enhanced wave pseudopotential was used to describe the ion nucleus and valence electron interactions[37,38]. A kinetic energy cutoff of 400 eV was chosen as the plane wave basis set. To focus solely on the interactions between the responsive gas molecules and the capture sites, we simplified the calculations and reduced the computational load by extracting the Cu-SBU_2 dimer surrounding the capture sites of **FZU-2** and **FZU-2NH_3** as the computational model (Supplementary Fig. 31). Given the positional disorder of $\{Cu_4O_{16}\}$ core within the $Cu_4@Nb_{29}$ SBUs, one specific configuration was selected for the calculations. The integration over the reciprocal space was performed using a Monkhorst model with a Γ-point. The atomistic structures and the difference charge densities are illustrated using VESTA[39]. The version of the Bader program used for Bader charge analysis is v1.05[40].

Data availability

The entries of CCDC 2026070, 2341510 and 2341511 contain the supplementary crystallographic data for **FZU-2**, **FZU-2NH$_3$**, and **FZU-2Recovered**. These data can be obtained free of charge at http://www.ccdc.cam.ac.uk/conts/retrieving.html or from the Cambridge Crystallographic Data Centre, 12, Union Road, Cambridge CB2 1EZ, U.K. Fax: (Internet) + 44-1223/336-033. E-mail: depos-it@ccdc.cam.ac.uk. The authors declare that all data supporting the findings of this study are available within the article (and Supplementary Information Files), or available from the corresponding author on request. Source data about all spectral characterization and trace NH$_3$ sensing experiments provided with this paper. Source data are provided with this paper.

References

1. Kim, I. et al. Holographic metasurface gas sensors for instantaneous visual alarms. *Sci. Adv.* **7**, eabe9943 (2021).
2. Lewis, A. & Edwards, P. Validate personal air-pollution sensors. *Nature* **535**, 29–31 (2016).
3. Ren, Y. et al. Synthesis of orthogonally assembled 3D cross-stacked metal oxide semiconducting nanowires. *Nat. Mater.* **19**, 203–211 (2019).
4. Zhang, X. et al. Managing nitrogen for sustainable development. *Nature* **528**, 51–59 (2015).
5. Erisman, J. W., Sutton, M. A., Galloway, J., Klimont, Z. & Winiwarter, W. How a century of ammonia synthesis changed the world. *Nat. Geosci.* **1**, 636–639 (2008).
6. Vasquez, K. Measuring atmospheric trace gases using mass spectrometry. *Nat. Rev. Earth Environ.* **2**, 305 (2021).
7. Yuan, H.-Y., Li, N.-X., Fan, W.-D., Cai, H. & Zhao, D. Metal-organic framework based gas sensors. *Adv. Sci.* **9**, 2104374 (2021).
8. Yi, J.-X., Chen, W.-J., Han, J. & Chen, D.-D. Sensitive and selective detection of plasticizer vapors with modified-SnO$_2$ hollow nanofibers for electrical fire warning. *Sens. Actuators B Chem.* **287**, 364–370 (2019).
9. Zhang, H. et al. A chemiresistive-potentiometric multivariate sensor for discriminative gas detection. *Nat. Commun.* **14**, 3495 (2023).
10. Freddi, S., Gonzalez, M. C. R., Carro, P., Sangaletti, L. & De Feyter, S. Chemical defect-driven response on graphene-based chemiresistors for sub-ppm ammonia detection. *Angew. Chem. Int. Ed.* **61**, e202200115 (2022).
11. Jung, Y. et al. Humidity-tolerant single-stranded DNA-functionalized graphene probe for medical applications of exhaled breath analysis. *Adv. Funct. Mater.* **27**, 1700068 (2017).
12. Zhang, T. et al. Engineering crystalline quasi-two-dimensional polyaniline thin film with enhanced electrical and chemiresistive sensing performances. *Nat. Commun.* **10**, 4255 (2019).
13. Yao, M. S. et al. A dual-ligand porous coordination polymer chemiresistor with modulated conductivity and porosity. *Angew. Chem. Int. Ed.* **59**, 172–176 (2019).
14. Shan, Z. et al. Topologically tunable conjugated metal-organic frameworks for modulating conductivity and chemiresistive properties for NH$_3$ sensing. *Angew. Chem. Int. Ed.* **63**, e202401679 (2024).
15. Feng, Q.-X., Huang, B.-Y. & Li, X.-G. Graphene-based heterostructure composite sensing materials for detection of nitrogen-containing harmful gases. *Adv. Funct. Mater.* **31**, 2104058 (2021).
16. Woellner, M. et al. Adsorption and detection of hazardous trace gases by metal-organic frameworks. *Adv. Mater.* **30**, 1704679 (2018).
17. Snyder, B. E. R. et al. A ligand insertion mechanism for cooperative NH$_3$ capture in metal-organic frameworks. *Nature* **613**, 287–291 (2023).
18. Rieth, A. J., Wright, A. M. & Dincă, M. Kinetic stability of metal-organic frameworks for corrosive and coordinating gas capture. *Nat. Rev. Mater.* **4**, 708–725 (2019).
19. Martin, N. P. & Nyman, M. Directional bonding in decaniobate inorganic frameworks. *Angew. Chem. Int. Ed.* **60**, 954–960 (2021).
20. Zhao, C.-C. et al. All-inorganic networks and tetramer based on tin (II)-containing polyoxometalates: tuning structural and spectral properties with lone-pairs. *J. Am. Chem. Soc.* **136**, 12085–12091 (2014).
21. Zhan, C.-H. et al. A metamorphic inorganic framework that can be switched between eight single-crystalline states. *Nat. Commun.* **8**, 14185 (2017).
22. Turo, M. J., Chen, L., Moore, C. E. & Schimpf, A. M. Co^{2+}-Linked [NaP$_5$W$_{30}$O$_{110}$]$^{14-}$: a redox-active metal oxide framework with high electron density. *J. Am. Chem. Soc.* **141**, 4553–4557 (2019).
23. Ma, B.-K. et al. A zeolitic octahedral metal oxide with ultra-microporosity for inverse CO$_2$/C$_2$H$_2$ separation at high temperature and humidity. *Angew. Chem. Int. Ed.* **61**, e202209121 (2022).
24. Khan, M. I., Yohannes, E. & Doedens, R. J. [M$_3$V$_{18}$O$_{42}$(H$_2$O)$_{12}$(XO$_4$)] ·24H$_2$O (M=Fe, Co; X=V, S): metal oxide based framework materials composed of polyoxovanadate clusters. *Angew. Chem. Int. Ed.* **38**, 1292–1294 (1999).
25. Wu, P.-X. et al. Giant polyoxoniobate-based inorganic molecular tweezers: metal recognitions, ion-exchange interactions and mechanism studies. *Angew. Chem. Int. Ed.* **62**, e202217926 (2023).
26. Liu, Y.-X. et al. Site differentiation strategy for selective strontium uptake and elution within an all-inorganic polyoxoniobate framework. *Nat. Commun.* **15**, 8896 (2024).
27. Nyman, M., Celestian, A. J., Parise, J. B., Holland, G. P. & Alam, T. M. Solid-state structural characterization of a rigid framework of lacunary heteropolyniobates. *Inorg. Chem.* **45**, 1043–1052 (2006).
28. Tsunashima, R. et al. The construction of high-nuclearity isopolyoxoniobates with pentagonal building blocks: [HNb$_{27}$O$_{76}$]$^{16-}$ and [H$_{10}$Nb$_{31}$O$_{93}$(CO$_3$)]$^{23-}$. *Angew. Chem. Int. Ed.* **49**, 113–116 (2010).
29. Brown, I. D. & Altermatt, D. Bond-valence parameters obtained from a systematic analysis of the inorganic crystal structure database. *Acta Crystallogr., Sect. B Struct. Sci.* **41**, 244–247 (1985).
30. Mozaffari Majd, M., Kordzadeh-Kermani, V., Ghalandari, V., Askari, A. & Sillanpää, M. Adsorption isotherm models: a comprehensive and systematic review (2010–2020). *Sci. Total Environ.* **812**, 151334 (2022).
31. Yang, J.-L. et al. Anatase porous titania nanosheets for resonant-gravimetric detection of ppb-level NO$_2$ at room-temperature. *Analyst* **146**, 4042–4048 (2021).
32. Yao, M.-S. et al. Van der Waals heterostructured MOF-on-MOF thin films: cascading functionality to realize advanced chemiresistive sensing. *Angew. Chem. Int. Ed.* **58**, 14915–14919 (2019).
33. Li, P. et al. Effect of polyoxometalates electron acceptor decoration on NO$_2$ sensing behavior of ZnS microspheres toward rapid and ultrahigh response. *Sensor. Actuators B Chem.* **426**, 137111 (2025).
34. Zhang, M. et al. First polyoxometalate-modified SnS$_2$ composite nanostructure gas sensor toward enhanced sensitivity and high selectivity for NO$_2$ detection. *Sensor. Actuators B Chem.* **409**, 135641 (2024).
35. Zhang, L. et al. Polyoxometalates/metal-organic frameworks-derived ZnO/ZnWO$_4$ nanoparticles for highly sensitive and selective ppb-level NO$_2$ detection. *Chem. Eng. J.* **499**, 156604 (2024).
36. Perdew, J. P., Burke, K. & Ernzerhof, M. Generalized gradient approximation made simple. *Phys. Rev. Lett.* **77**, 3865–3868 (1996).
37. Kresse, G. & Joubert, D. From ultrasoft pseudopotentials to the projector augmented-wave method. *Phys. Rev. B* **59**, 1758–1775 (1999).
38. Blochl, P. E. Projector augmented-wave method. *Phys. Rev. B* **50**, 17953–17979 (1994).
39. Momma, K. & Izumi, F. VESTA 3 for three-dimensional visualization of crystal, volumetric and morphology data. *J. Appl. Crystallogr.* **44**, 1272–1276 (2011).
40. Tang, W., Sanville, E. & Henkelman, G. A grid-based Bader analysis algorithm without lattice bias. *J. Phys. Condens. Matter* **21**, 084204 (2009).

Acknowledgements

This work was supported by the National Natural Science Foundation of China (22371045, 22371046). C.S. was supported by the NSFC with No. 22371045, and S.-T.Z. was supported by the NSFC with No. 22371046, We thank Prof. Gang Xu from Fujian Institute of Research on the Structure of Matter, CAS for microgravimetric experiment.

Author contributions

C.S., S.-T.Z conceived the idea and prepared the manuscript. Z.-W.G., Y.-H.Y. conducted the characterizations and detecting tests. Y.C., Y.-Y.L., and X.-X.L. contributed to the discussion. All authors have given approval to the final version of the manuscript.

Competing interests

The authors declare no competing interests.

Additional information

Supplementary information The online version contains supplementary material available at https://doi.org/10.1038/s41467-025-61845-4.

Correspondence and requests for materials should be addressed to Cai Sun or Shou-Tian Zheng.

Peer review information *Nature Communications* thanks Shaobin Li, and the other, anonymous, reviewer(s) for their contribution to the peer review of this work. A peer review file is available.

Reprints and permissions information is available at http://www.nature.com/reprints

Publisher's note Springer Nature remains neutral with regard to jurisdictional claims in published maps and institutional affiliations.

Open Access This article is licensed under a Creative Commons Attribution-NonCommercial-NoDerivatives 4.0 International License, which permits any non-commercial use, sharing, distribution and reproduction in any medium or format, as long as you give appropriate credit to the original author(s) and the source, provide a link to the Creative Commons licence, and indicate if you modified the licensed material. You do not have permission under this licence to share adapted material derived from this article or parts of it. The images or other third party material in this article are included in the article's Creative Commons licence, unless indicated otherwise in a credit line to the material. If material is not included in the article's Creative Commons licence and your intended use is not permitted by statutory regulation or exceeds the permitted use, you will need to obtain permission directly from the copyright holder. To view a copy of this licence, visit http://creativecommons.org/licenses/by-nc-nd/4.0/.

© The Author(s) 2025